Supporting Information

Zinc niobate materials: crystal structures, energy-storage capabilities and working mechanisms

Xiangzhen Zhu[a,b], Haijie Cao[a,], Renjie Li[b], Qingfeng Fu[b], Guisheng Liang[b], Yongjun Chen[b], Lijie Luo[b], Chunfu Lin[a,b,*], Xiu Song Zhao[b,c]*

[a] *Institute of Materials for Energy and Environment, School of Materials Science and Engineering, Qingdao University, Qingdao 266071, China*

[b] *State Key Laboratory of Marine Resource Utilization in South China Sea, School of Materials Science and Engineering, Hainan University, Haikou 570228, China*

[c] *School of Chemical Engineering, The University of Queensland, St Lucia, Brisbane, QLD 4072, Australia*

[*] *Corresponding authors. E-mail addresses: caohj1582@hotmail.com (H. Cao), linchunfu@qdu.edu.cn (C. Lin).*

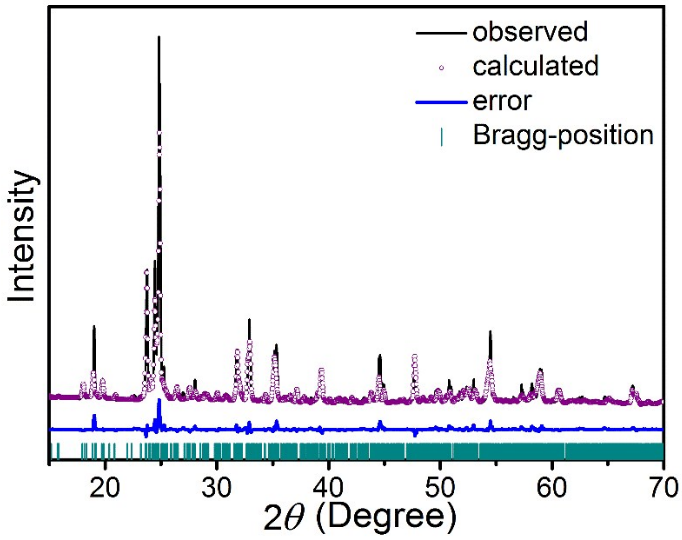

Fig. S1. XRD spectrum with Retveld refinement of $W_5Nb_{16}O_{55}$.

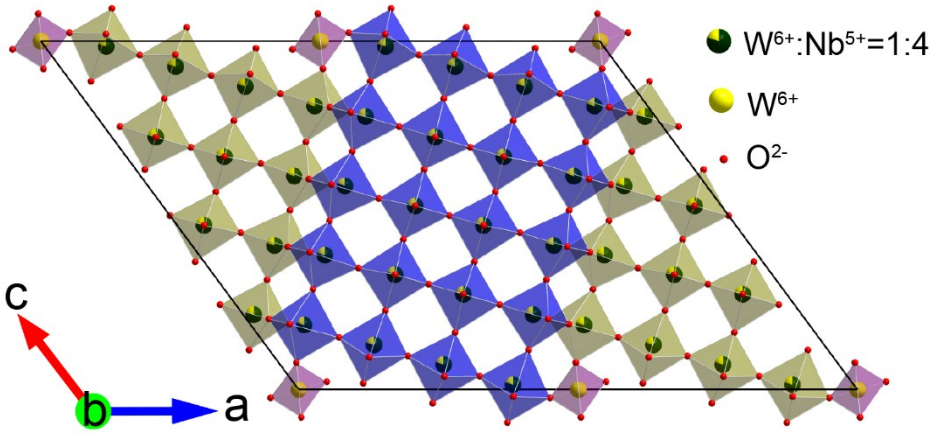

Fig. S2. Crystal structure of $W_5Nb_{16}O_{55}$.

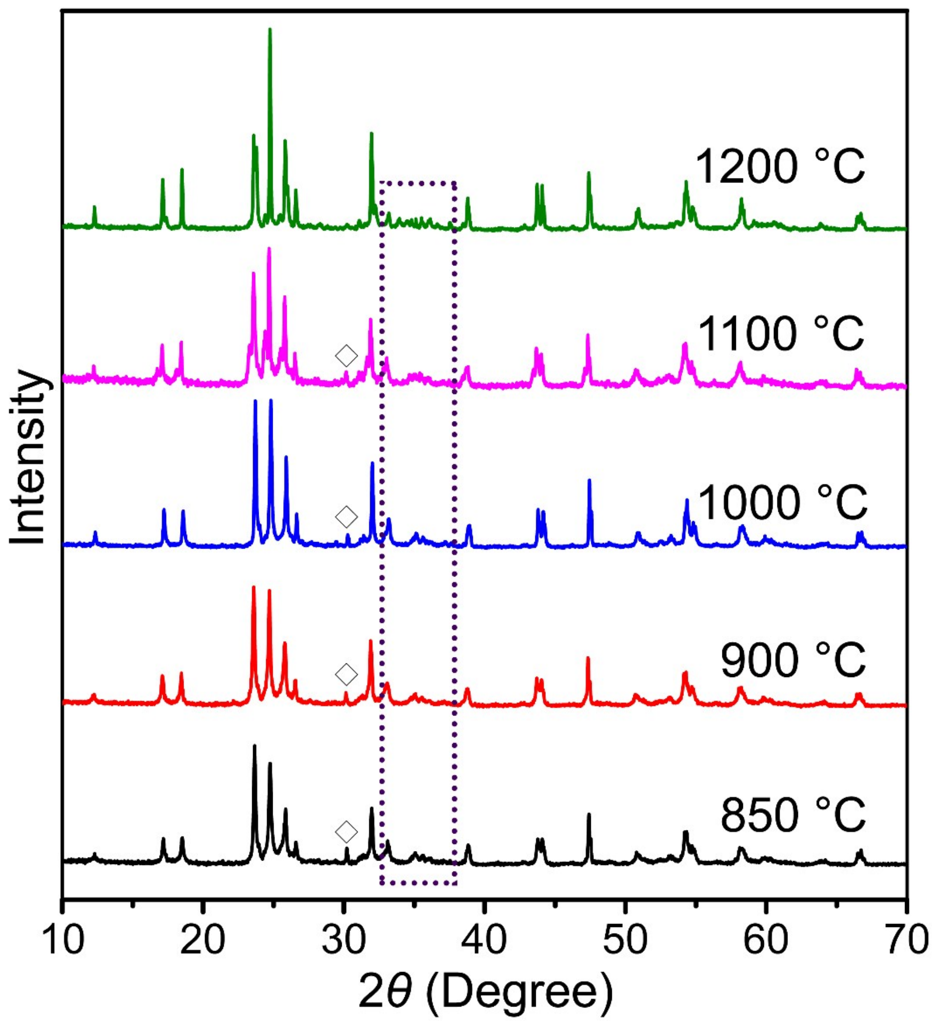

Fig. S3. XRD spectra of $Zn_2Nb_{34}O_{87}$-N sintered at 850, 900, 1000, 1100 and 1200 °C

(◇: $ZnNb_2O_6$).

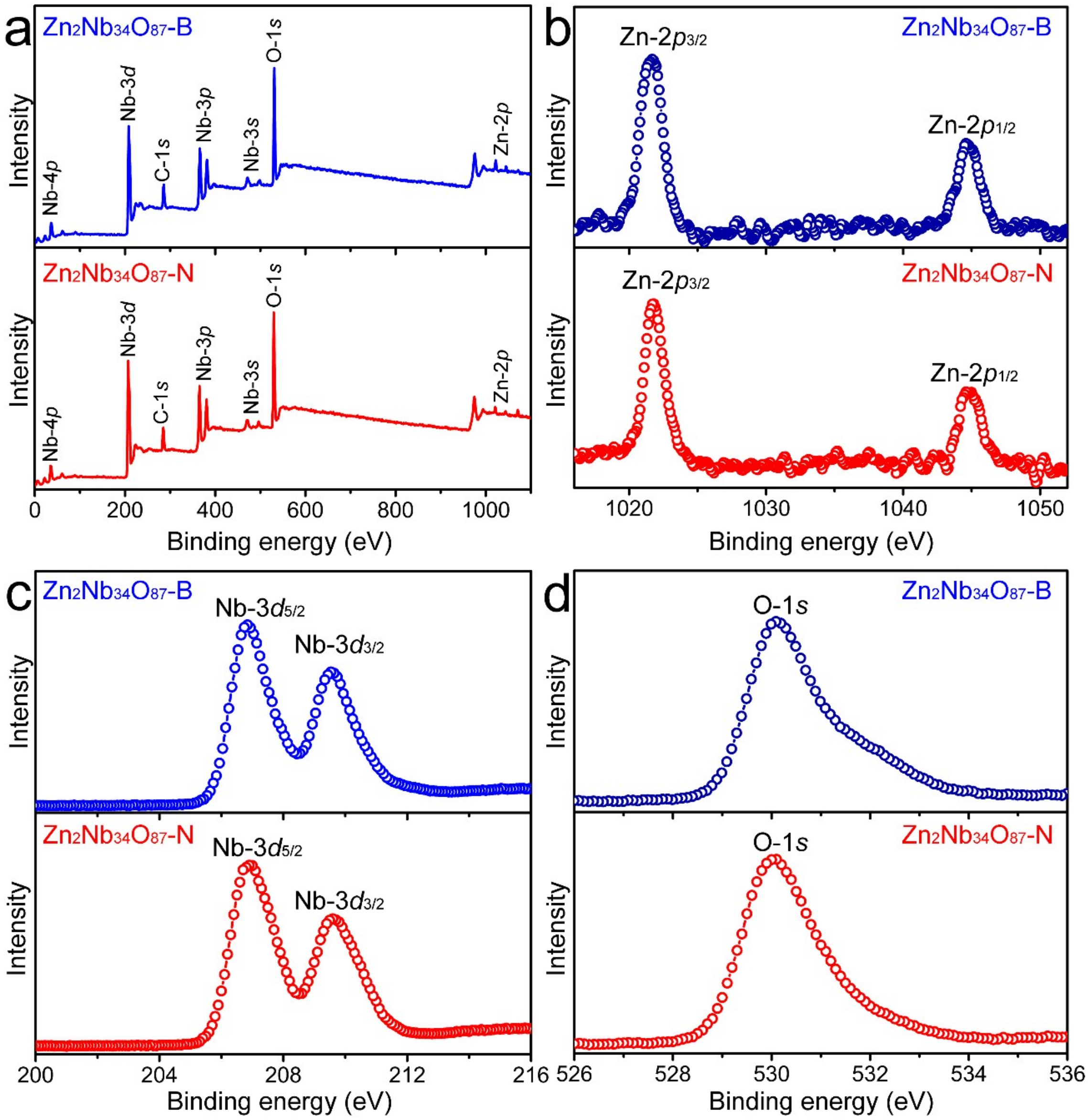

Fig. S4. (a) XPS survey spectra of $Zn_2Nb_{34}O_{87}$-B and $Zn_2Nb_{34}O_{87}$-N. XPS spectra of (b) Zn, (c) Nb and (d) O elements in $Zn_2Nb_{34}O_{87}$-B and $Zn_2Nb_{34}O_{87}$-N.

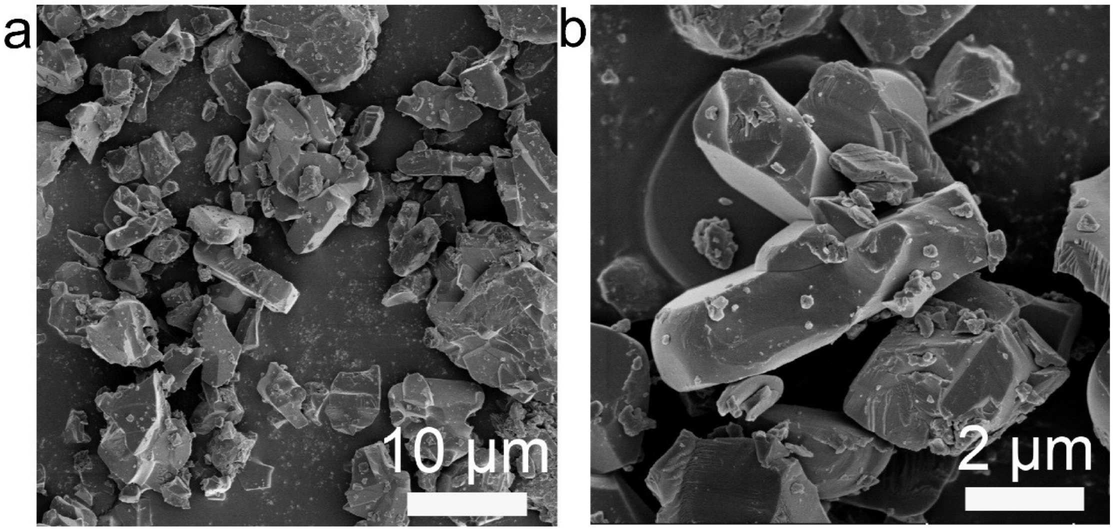

Fig. S5. (a, b) FESEM images of $Zn_2Nb_{34}O_{87}$-B.

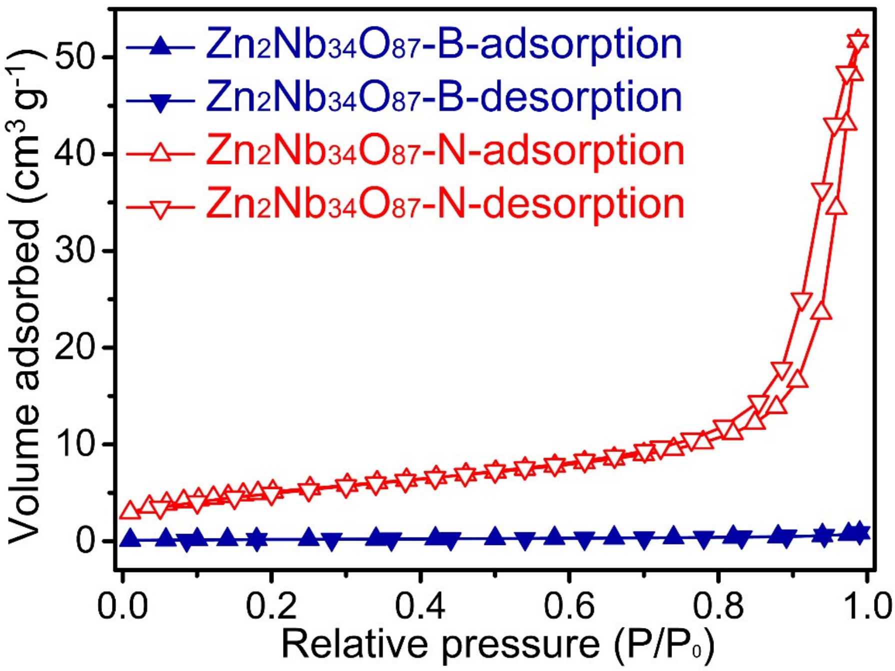

Fig. S6. N_2 adsorption–desorption isotherms of $Zn_2Nb_{34}O_{87}$-B and $Zn_2Nb_{34}O_{87}$-N.

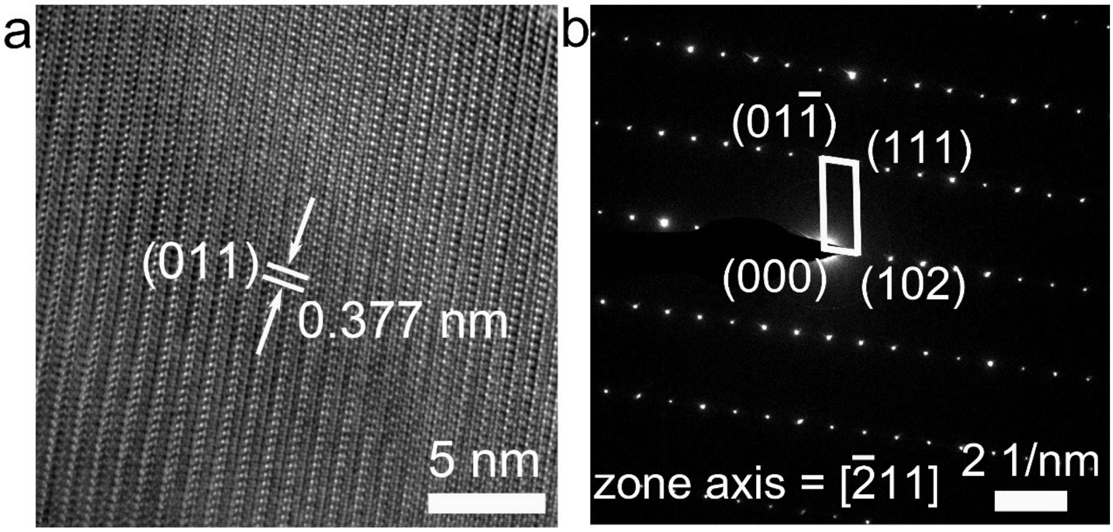

Fig. S7. (a) HRTEM image and (b) SAED pattern of $Zn_2Nb_{34}O_{87}$-B.

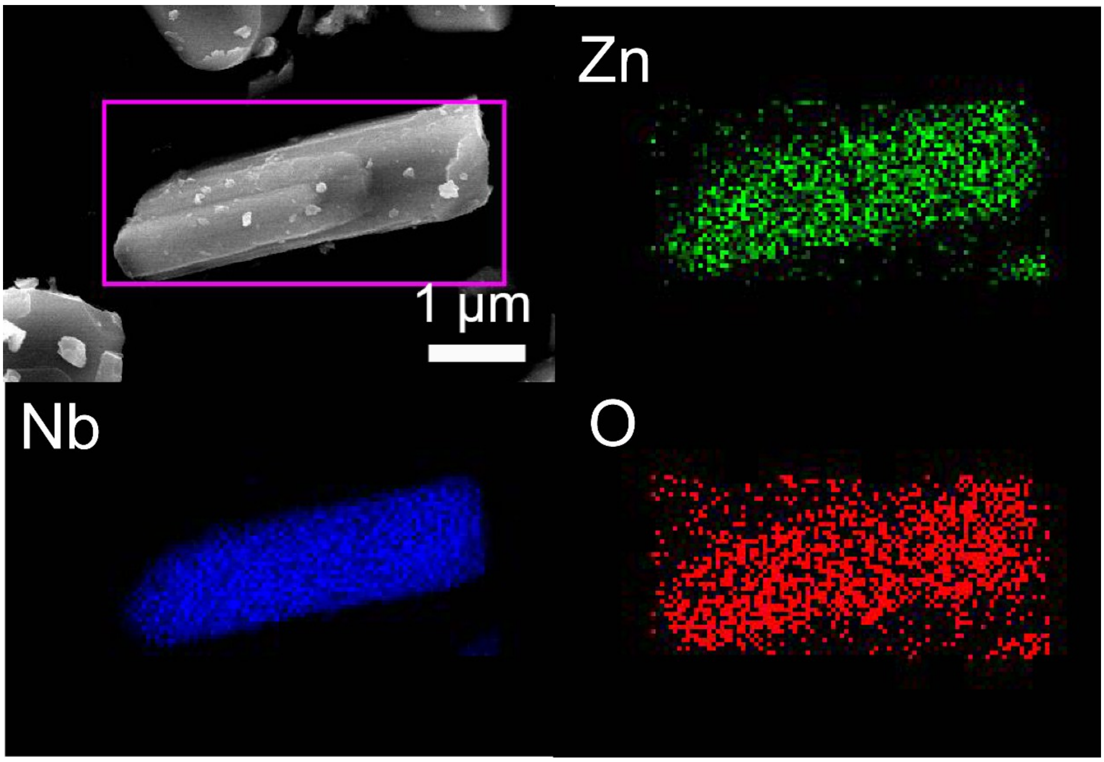

Fig. S8. EDX mapping images of $Zn_2Nb_{34}O_{87}$-B.

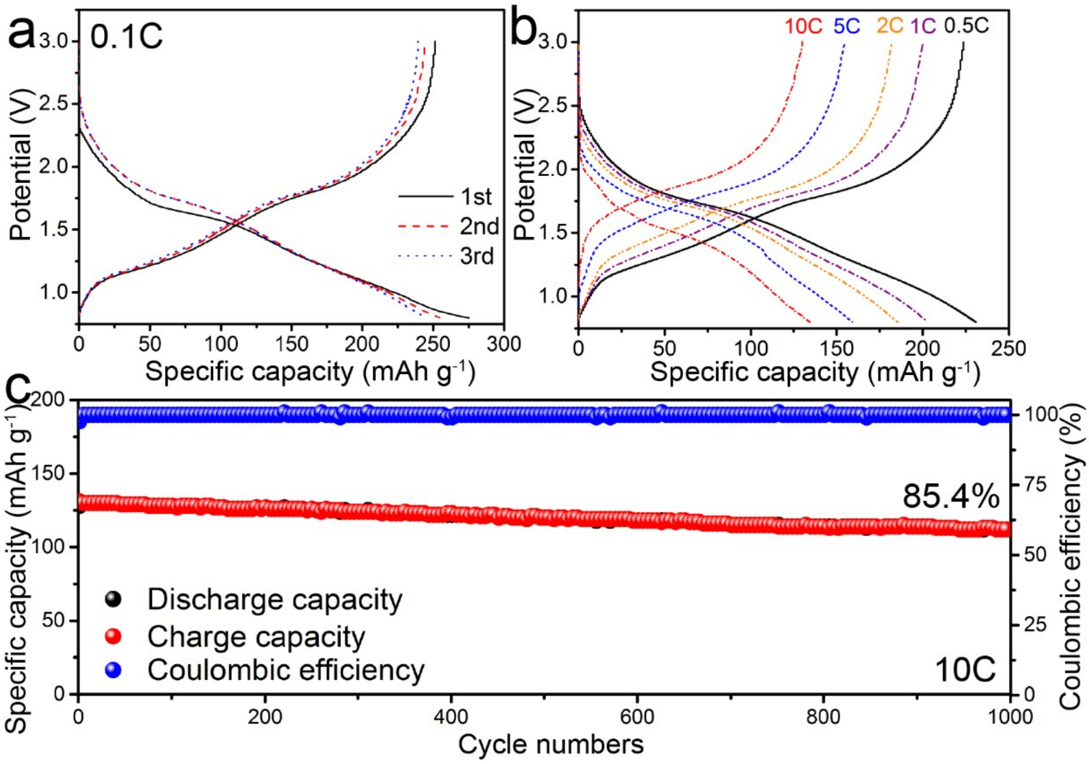

Fig. S9. Electrochemical performance of $W_5Nb_{16}O_{55}$/Li cell (the fabrication process of the $W_5Nb_{16}O_{55}$/Li cell is the same as that of the $Zn_2Nb_{34}O_{87}$/Li cell): discharge–charge curves at (a) 0.1C and (b) different current rates, and (c) cyclability at 10C over 1000 cycles.

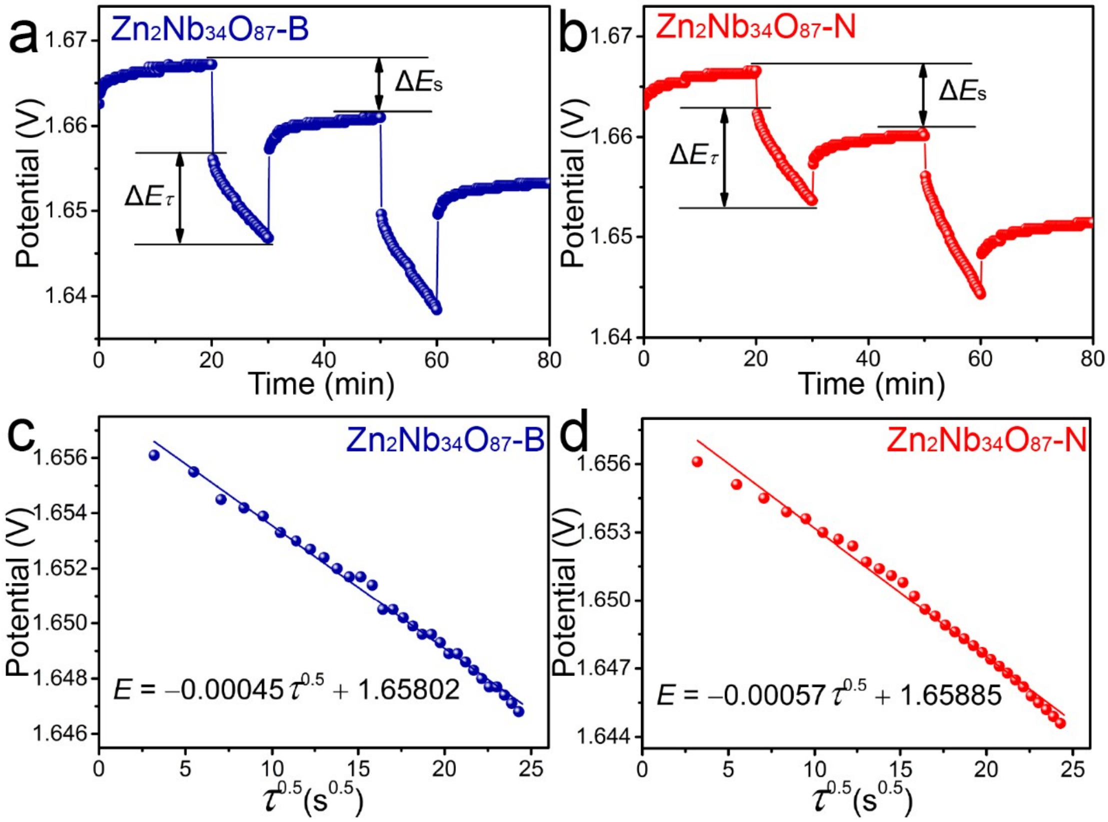

Fig. S10. *E versus T* curves for a single step in GITT experiment of (a) $Zn_2Nb_{34}O_{87}$-B and (b) $Zn_2Nb_{34}O_{87}$-N. Linear behavior of *E versus* $\tau^{0.5}$ relationship during a typical titration in (c) $Zn_2Nb_{34}O_{87}$-B and (d) $Zn_2Nb_{34}O_{87}$-N.

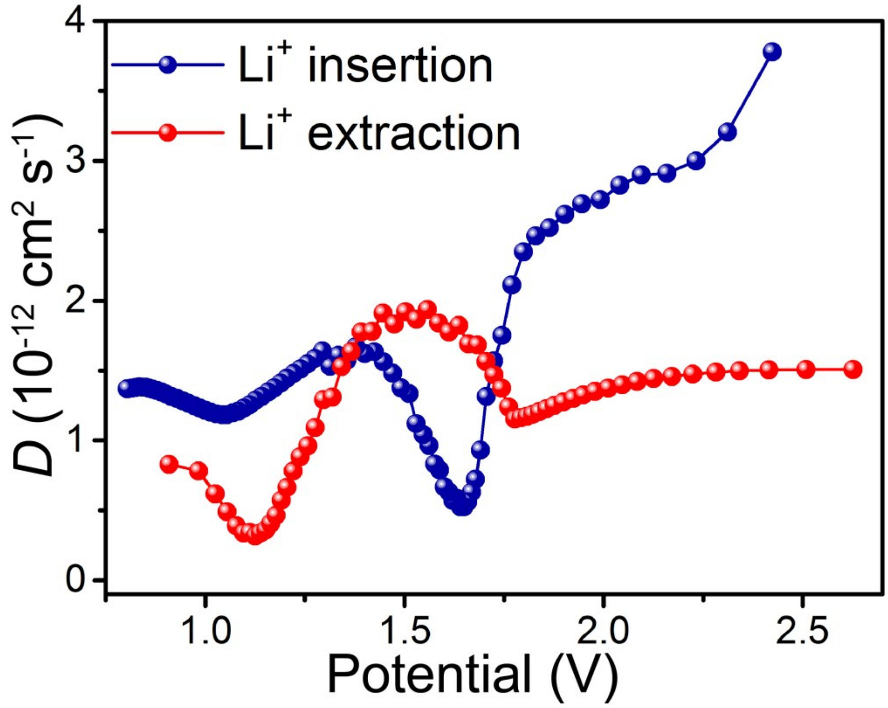

Fig. S11. Variation in Li^+ diffusion coefficient of $W_5Nb_{16}O_{55}$ calculated from GITT.

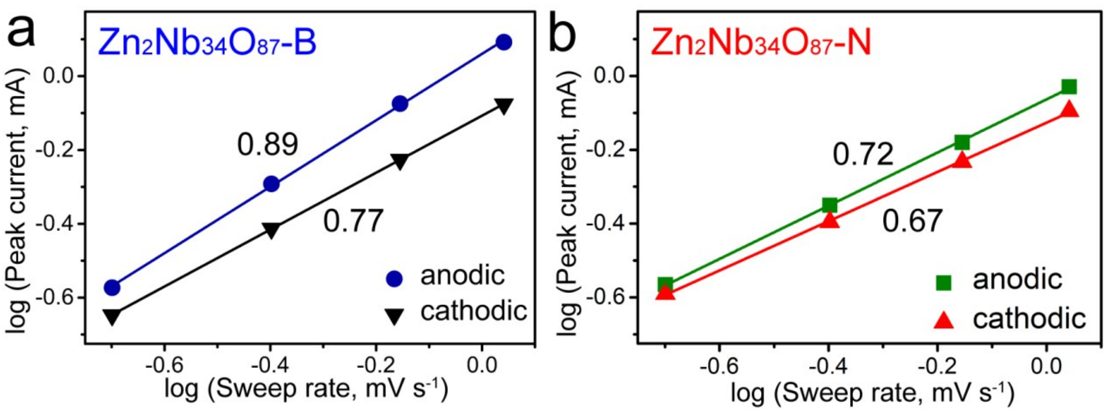

Fig. S12. Determination of *b*-values of (a) $Zn_2Nb_{34}O_{87}$-B and (b) $Zn_2Nb_{34}O_{87}$-N using relationship between logarithm of peak current and logarithm of sweep rate.

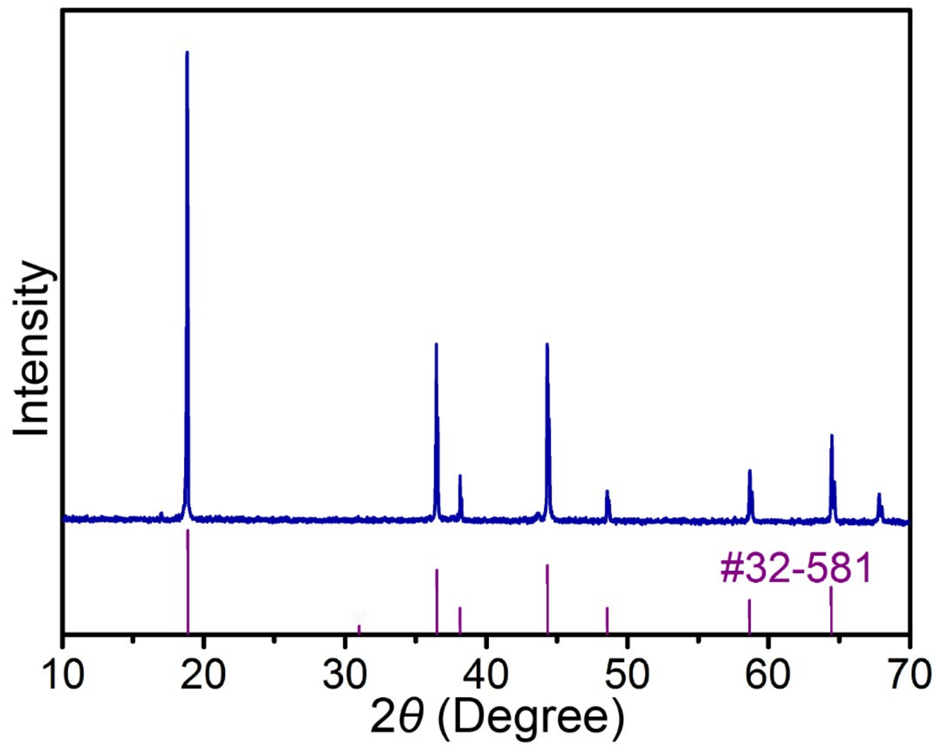

Fig. S13. XRD spectrum of $LiNi_{0.5}Mn_{1.5}O_4$.

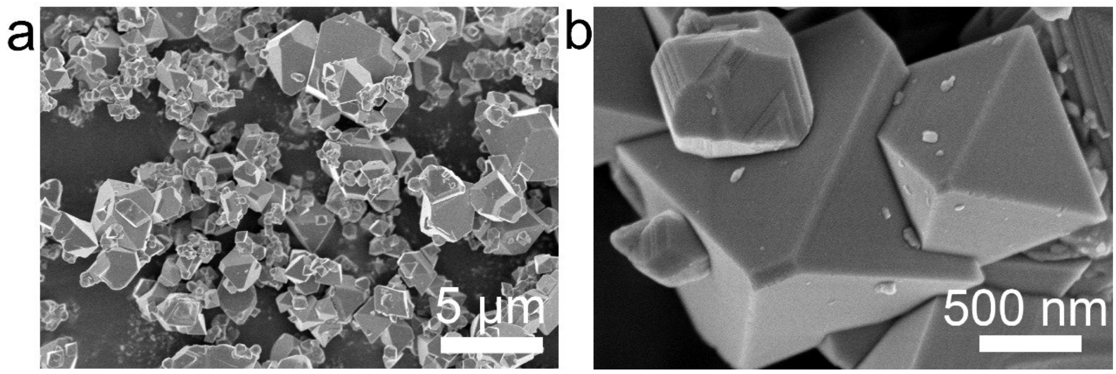

Fig. S14. (a) low-magnification and (b) high-magnification FESEM images of $LiNi_{0.5}Mn_{1.5}O_4$.

Table S1. Results of crystal analyses by Rietveld refinements in $Zn_2Nb_{34}O_{87}$-B (orthorhombic) with *Amma* space group, $Zn_2Nb_{34}O_{87}$-N (monoclinic) with *A2/m* space group, and $W_5Nb_{16}O_{55}$ (monoclinic) with space group of *C2*.

material	*a* (nm)	***b* (nm)**	*c* (nm)	*α*,*γ* (°)	*β* (°)	*V* (nm^3)
$Zn_2Nb_{34}O_{87}$-B	2.871489 (11)	**0.382780 (2)**	2.065497 (8)	90	90	2.270295 (252)
$Zn_2Nb_{34}O_{87}$-N	1.561179 (13)	**0.383217 (2)**	2.066574 (14)	90	113.089 (6)	1.137327 (177)
$W_5Nb_{16}O_{55}$	2.970832 (41)	**0.381905 (4)**	2.314088 (39)	90	126.546 (6)	2.109270 (547)

Table S2. Fractional atomic parameters of $Zn_2Nb_{34}O_{87}$-B with space group of *Amma*.

atom	site	*x*	*y*	*z*
Zn1	8*f*	0.046206	0	0.040711
Nb1	8*f*	0.046206	0	0.040711
Nb2	8*f*	0.050236	0	0.666035
Nb3	8*f*	0.046842	0	0.856061
Nb4	8*f*	0.183754	0	0.037185
Nb5	8*f*	0.183215	0	0.668334
Nb6	8*f*	0.181841	0	0.854427
O1	4*c*	0.250000	0	0.031265
O2	4*c*	0.250000	0	0.679758
O3	4*c*	0.250000	0	0.853859
O4	8*f*	0.056530	0	0.541091
O5	8*f*	0.035402	0	0.144409
O6	8*f*	0.036660	0	0.753260
O7	8*f*	0.039926	0	0.334375
O8	8*f*	0.024082	0	0.957767
O9	8*f*	0.114317	0	0.033460
O10	8*f*	0.111637	0	0.663379
O11	8*f*	0.109285	0	0.849359
O12	8*f*	0.188744	0	0.573336
O13	8*f*	0.180203	0	0.143517
O14	8*f*	0.173937	0	0.759216
O15	8*f*	0.183017	0	0.349929
O16	8*f*	0.175322	0	0.953713

Table S3. Fractional atomic parameters of $Zn_2Nb_{34}O_{87}$-N with space group of *A2/m*.

atom*	site	*x*	*y*	*z*
M1	4*i*	0.094900	0	0.068931
M2	4*i*	0.093568	0	0.688770
M3	4*i*	0.095237	0	0.887346
M4	4*i*	0.374830	0	0.148083
M5	4*i*	0.364012	0	0.778313
M6	4*i*	0.356387	0	0.955579
O1	2*d*	0.500000	0	0
O2	4*i*	0.070218	0	0.166963
O3	4*i*	0.072770	0	0.354527
O4	4*i*	0.084555	0	0.582856
O5	4*i*	0.082229	0	0.784255
O6	4*i*	0.131786	0	0.992904
O7	4*i*	0.214648	0	0.099463
O8	4*i*	0.221544	0	0.730309
O9	4*i*	0.209007	0	0.920269
O10	4*i*	0.343510	0	0.062637
O11	4*i*	0.350924	0	0.253865
O12	4*i*	0.368872	0	0.387533
O13	4*i*	0.370454	0	0.664701
O14	4*i*	0.359728	0	0.860083
O15	4*i*	0.495672	0	0.192593

*M = 1/18 Zn^{2+} + 17/18 Nb^{5+}

Table S4. Comparisons of reversible/theoretical capacity of $Zn_2Nb_{34}O_{87}$-B/ $Zn_2Nb_{34}O_{87}$-N with previously reported insertion negative electrode materials.

material	theoretical capacity (mAh g^{-1})	capacity in reports (mAh g^{-1})	reference
$Zn_2Nb_{34}O_{87}$-N	389	310	this work
$Zn_2Nb_{34}O_{87}$-B	389	284	this work
graphite	372	310	[S1]
$Li_4Ti_5O_{12}$	175	169	[S2]
$TiNb_2O_7$	388	281	[S3]
$Ti_2Nb_{10}O_{29}$	396	247	[S4]
$TiNb_{24}O_{62}$	402	296	[S5]
Nb_2O_5	403	210	[S6]
$FeNb_{11}O_{29}$	400	270	[S7]
$GaNb_{11}O_{29}$	379	264	[S8]
$GeNb_{18}O_{47}$	386	217	[S9]
PNb_9O_{25}	381	200	[S10]
VNb_9O_{25}	416	220	[S11]
$WNb_{12}O_{33}$	302	228	[S12]
$W_5Nb_{16}O_{55}$	302	225	[S13]
$BaNb_{3.6}O_{10}$	306	264	[S14]
$K_2Nb_8O_{21}$	371	281	[S15]
$W_9Nb_8O_{47}$	289	238	[S16]
$W_{16}Nb_{18}O_{93}$	228	195	[S17]

Table S5. Comparisons of electrochemical performance of $Zn_2Nb_{34}O_{87}$-B and $Zn_2Nb_{34}O_{87}$-N with previously reported niobium-based oxide negative electrode materials.

material	current rate	rate performance (mAh g^{-1})	reference
$Zn_2Nb_{34}O_{87}$-N	10C	~197 at 1000th cycles	this work
$Zn_2Nb_{34}O_{87}$-B	10C	~140 at 1000th cycles	this work
$W_5Nb_{16}O_{55}$ micron-sized particles	10C	~111 at 1000th cycles	Fig. S9c
$TiNb_2O_7$ nanoparticles	10C	~123 at 500th cycles	[S18]
$TiNb_2O_7$ nanofibers	5C	~170 at 500th cycles	[S19]
$TiNb_2O_7$ nanorods	10C	~140 at 100th cycles	[S20]
three-dimensional (3D) ordered macroporous $TiNb_2O_7$	10C	~87 at 100th cycles	[S21]
$Cu_{0.02}Ti_{0.94}Nb_{2.04}O_7$	10C	~180 at 1000th cycles	[S22]
$Ti_2Nb_{10}O_{29}$ hollow nanofibers	10C	~123 at 500th cycles	[S23]
porous $Ti_2Nb_{10}O_{29}$ nanospheres	10C	~141 at 1000th cycles	[S24]
porous $TiNb_{24}O_{62}$ microspheres	10C	~183 at 500th cycles	[S5]
$WNb_{12}O_{33}$ nanowires	3C	~140 at 700th cycles	[S12]
$GeNb_{18}O_{47}$ nanofibers	2C	~162 at 200th cycles	[S9]
VNb_9O_{25} nanoribbons	3C	~132 at 500th cycles	[S11]
$W_9Nb_8O_{47}$ nanofibers	5C	~113 at 1000th cycles	[S16]
$GaNb_{11}O_{29}$ nanowebs	10C	~153 at 1000th cycles	[S8]

References

[S1]Y.P. Wu, E. Rahm, R. Holze, Carbon anode materials for lithium ion batteries, J. Power Sources 114 (2003) 228–236.

[S2]T.F. Yi, L.J. Jiang, J. Shu, C.B. Yue, R.S. Zhu, H.B. Qiao, Recent development and application of $Li_4Ti_5O_{12}$ as anode material of lithium ion battery, J. Phys. Chem. Solids 71 (2010) 1236–1242.

[S3]J.T. Han, Y.H. Huang, J.B. Goodenough, New anode framework for rechargeable lithium batteries, Chem. Mater. 23 (2011) 2027–2029.

[S4]X.Y. Wu, J. Miao, W.Z. Han, Y.S. Hu, D.F. Chen, J.S. Lee, J. Kim, L.Q. Chen, Investigation on $Ti_2Nb_{10}O_{29}$ anode material for lithium-ion batteries, Electrochem. Commun. 25 (2012) 39–42.

[S5]C. Yang, S.J. Deng, C.F. Lin, S.W. Lin, Y.J. Chen, J.B. Li, H. Wu, Porous $TiNb_{24}O_{62}$ microspheres as high-performance anode materials for lithium-ion batteries of electric vehicles, Nanoscale 8 (2016) 18792–18799.

[S6]S.F. Lou, X.Q. Cheng, L. Wang, J.L. Gao, Q. Li, Y.L. Ma, Y.Z. Gao, P.J. Zuo, C.Y. Du, G.P. Yin, High-rate capability of three-dimensionally ordered macroporous T-Nb_2O_5 through Li^+ intercalation pseudocapacitance, J. Power Sources 361 (2017) 80–86.

[S7]X.M. Lou, Z.H. Xu, Z.B. Luo, C.F. Lin, C. Yang, H. Zhao, P. Zheng, J.B. Li, N. Wang, Y.J. Chen, H. Wu, Exploration of $Cr_{0.2}Fe_{0.8}Nb_{11}O_{29}$ as an advanced anode material for lithium-ion batteries of electric vehicles, Electrochim. Acta 245 (2017) 482–488.

[S8]X.M. Lou, Q.F. Fu, J. Xu, X. Liu, C.F. Lin, J.X. Han, Y.P. Luo, Y.J. Chen, X.Y. Fan, J.B. Li, $GaNb_{11}O_{29}$ nanowebs as high-performance anode materials for lithium-ion batteries, ACS Appl. Nano Mater. 1 (2018) 183–190.

[S9]F.M. Ran, X. Cheng, H.X. Yu, R.T. Zheng, T.T. Liu, X.F. Li, N. Ren, M. Shui, J. Shu, Nano-structured $GeNb_{18}O_{47}$ as novel anode host with superior lithium storage performance, Electrochim. Acta 282 (2017) 634–641.

[S10]S. Patoux, M. Dolle, G. Rousse, C. Masquelier, A reversible lithium intercalation process in an ReO_3-type structure $PbNb_9O_{25}$, J. Electrochem. Soc. 149 (2002) A391–A400.

[S11]S.S. Qian, H.X. Yu, L. Yan, H.J. Zhu, X. Cheng, Y. Xie, N.B. Long, M. Shui, J. Shu, High-rate long-life pored nanoribbon VNb_9O_{25} built by interconnected ultrafine nanoparticles as anode for lithium-ion batteries, ACS Appl Mater. Interfaces 9 (2017) 30608–30616.

[S12]L. Yan, H. Lan, H.X. Yu, S.S. Qian, X. Cheng, N.B. Long, R.F. Zhang, M. Shui, J. Shu, Electrospun $WNb_{12}O_{33}$ nanowires: superior lithium storage capability and their working mechanism, J. Mater. Chem. A 5 (2017) 8972–8980.

[S13]K.J. Griffith, K.M. Wiaderek, G. Cibin, L.E. Marbella, C.P. Grey, Niobium tungsten oxides for high-rate lithium-ion energy storage, Nature 559 (2018) 556–563.

[S14]X. Cheng, S.S. Qian, H.X. Yu, H.J. Zhu, Y. Xie, R.T. Zheng, T.T. Liu, M. Shui, J. Shu, $BaNb_{3.6}O_{10}$ nanowires with superior electrochemical performance towards ultrafast and highly stable lithium storage, Energy Storage Mater. 16 (2019) 400–410.

[S15]X. Cheng, H.J. Zhu, H.X. Yu, W.Q. Ye, R.T. Zheng, T.T. Liu, N. Peng, M. Shui, J. Shu, $K_2Nb_8O_{21}$ nanotubes with superior electrochemical performance for ultrastable lithium storage, J. Mater. Chem. A 6 (2018) 8620–8632.

[S16]L. Yan, X. Cheng, H.X. Yu, H.J. Zhu, T.T. Liu, R.T. Zheng, R.F. Zhang, M. Shui, J. Shu, Ultrathin $W_9Nb_8O_{47}$ nanofibers modified with thermal NH_3 for superior electrochemical energy storage, Energy Storage Mater. 14 (2018) 159–168.

[S17]W.Q. Ye, H.X. Yu, X. Cheng, H.J. Zhu, R.T. Zheng, T.T. Liu, N.B. Long, M. Shui, J. Shu, Highly efficient lithium container based on non-Wadsley-Roth structure $Nb_{18}W_{16}O_{93}$ nanowires for electrochemical energy storage, Electrochim. Acta 292 (2018) 331–338.

[S18]S.F. Lou, Y.L. Ma, X.Q. Cheng, J.L. Gao, Y.Z. Gao, P.J. Zuo, C.Y. Du, G.P. Yin, Facile synthesis of nanostructured $TiNb_2O_7$ anode materials with superior performance for high-rate lithium ion batteries, Chem. Commun. 51 (2015) 17293–17296.

[S19]H. Park, T. Song, U. Paik, Porous $TiNb_2O_7$ nanofibers decorated with conductive $Ti_{1-x}Nb_xN$ bumps as a high power anode material for Li-ion batteries, J. Mater. Chem. A 3 (2015) 8590–8596.

[S20]L. Hu, C.F. Lin, C.H. Wang, C. Yang, J.B. Li, Y.J. Chen, S.W. Lin, $TiNb_2O_7$ nanorods as a novel anode materials for secondary lithium-ion batteries. Funct. Mater. Lett. 9 (2016) 1642004.

[S21]S.F. Lou, X.Q. Cheng, Y. Zhao, A. Lushington, J.L. Gao, Q. Li, P.J. Zuo, B.Q. Wang, Y.Z. Gao, Y.L. Ma, C.Y. Du, G.P. Yin, X.L. Sun, Superior performance of ordered macroporous $TiNb_2O_7$ anodes for lithium ion batteries: understanding from the structural and pseudocapacitive insights on achieving high rate capability, Nano Energy 34 (2017) 15–25.

[S22]C. Yang, C.F. Lin, S.W. Lin, Y.J. Chen, J.B. Li, $Cu_{0.02}Ti_{0.94}Nb_{2.04}O_7$: an advanced anode material for lithium-ion batteries of electric vehicles, J. Power Sources 328 (2016) 336–344.

[S23]Q.F. Fu, J.R. Hou, R.H. Lu, C.F. Lin, Y. Ma, J.B. Li, Y.J. Chen, Electrospun $Ti_2Nb_{10}O_{29}$ hollow nanofibers as high-performance anode materials for lithium-ion batteries, Mater. Lett. 214 (2018) 60–63.

[S24]S.F. Lou, X.Q. Cheng, J.L. Gao, Q. Li, L. Wang, Y. Cao, Y.L. Ma, P.J. Zuo, Y.Z. Gao, C.Y. Du, H. Huo, G.P. Yin, Pseudocapacitive Li^+ intercalation in porous $Ti_2Nb_{10}O_{29}$ nanospheres enables ultra-fast lithium storage, Energy Storage Mater. 11 (2018) 57–66.